THE JOURNAL OF PHYSICAL CHEMISTRY B

Article

pubs.acs.org/JPCB

Distinct Helix Propensities and Membrane Interactions of Human and Rat IAPP$_{1-19}$ Monomers in Anionic Lipid Bilayers

Cong Guo,[†] Sébastien Côté,[‡] Normand Mousseau,[‡] and Guanghong Wei*[,†]

[†]State Key Laboratory of Surface Physics, Key Laboratory for Computational Physical Sciences (MOE), and Department of Physics, Fudan University, 220 Handan Road, Shanghai 200433, China

[‡]Département de Physique and Groupe de recherche sur les protéines membranaires (GEPROM), Université de Montréal, C.P. 6128, succursale Centre-ville, Montréal, Québec, Canada

Supporting Information

ABSTRACT: Islet amyloid polypeptide, IAPP or amylin, is a 37-residue peptide hormone coexpressed with insulin by pancreatic β-cells. The aggregation of human IAPP (hIAPP) into amyloid deposits is associated with type II diabetes. Substantial evidence suggests that the interaction of anionic membranes with hIAPP may facilitate peptide aggregation and the N-terminal 1−19 fragment (IAPP$_{1-19}$) plays an important role in peptide−membrane interaction. As a first step to understand how structural differences between human and rat IAPP peptides in membranes may influence the later oligomerization process, we have investigated the structures and orientations of hIAPP$_{1-19}$ and the less toxic rIAPP$_{1-19}$ (i.e., the H18R mutant of hIAPP$_{1-19}$) monomers in anionic POPG bilayers by performing replica exchange molecular dynamics (REMD) simulations. On the basis of ∼20 μs REMD simulations started from a random coil conformation of the peptide placed in water, we find that unfolded h(r)IAPP$_{1-19}$ can insert into the bilayers and the membrane-bound peptide stays mainly at the lipid head−tail interface. hIAPP$_{1-19}$ displays higher helix propensity than rIAPP$_{1-19}$, especially in the L12−L16 region. The helix is oriented parallel to the bilayer surface and buried in the membrane 0.3−0.8 nm below the phosphorus atoms, consistent with previous electron paramagnetic resonance data. The helical conformation is an amphiphilic helix with its hydrophilic and hydrophobic faces pointing, respectively, to the lipid head and tail regions. The H18R substitution enhances the electrostatic interactions of IAPP$_{1-19}$ with the membrane, while it weakens the intrapeptide interactions crucial for helix formation, thus leading to lower helix propensity of rIAPP$_{1-19}$. Implications of our simulation results on the membrane-mediated IAPP$_{1-19}$ oligomerization are discussed.

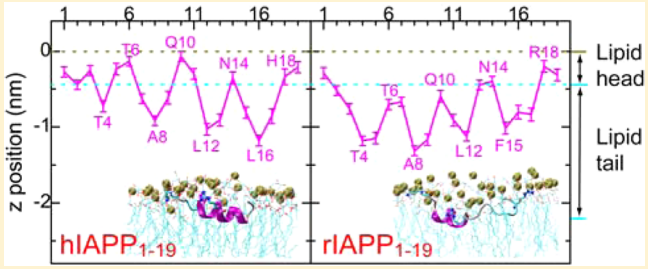

INTRODUCTION

Human islet amyloid polypeptide (hIAPP), also referred to amylin, is the protein component of amyloid fibrils found in individuals with type II diabetes.[1] The aggregates of hIAPP are found in over 90% of diabetics but only in a minority of nondiabetic subjects.[2] IAPP is a 37-residue peptide coexpressed with insulin by pancreatic β-cells. Its native form contains an amidated C-terminus and an intramolecular disulfide bridge between Cys2 and Cys7. It was reported that hIAPP has a strong cytotoxic effect on β-cells, while the nonaggregating rat IAPP (rIAPP) has little influence on β-cell survival rates even when massively overexpressed.[3] Previous experimental studies suggested that the IAPP monomer adopts primarily random coil conformations in aqueous solution.[4−7] After binding to the membrane surface,[8] IAPP transiently adopts helical structures before aggregating into amyloid fibrils.[4−6,9] The fibrillation of IAPP is highly accelerated in the presence of lipid bilayers, especially those composed of anionic phospholipids.[4,10,11] Accumulating evidence has shown that the most toxic species are early formed oligomers instead of mature amyloid fibrils.[12,13] Several mechanisms behind cytotoxicity have been proposed, among which the membrane disruption hypothesis predominates.[3,14−16] Toxic oligomers were reported to cause significant disruption of the phospholipid membrane in both model membranes and in cells through either the formation of ion channels or a nonspecific general disruption of lipid bilayers.[17−19]

The amino acid sequence of IAPP can be divided into three regions: the N-terminal 1−19 region, the primary amyloidogenic 20−29 region, and the C-terminal 30−37 region that can enhance amyloid formation.[8,20] The N-terminal 1−19 region has been reported to play an important role in fibrillogenesis and membrane disruption. In aqueous solution, this region influences the overall kinetics of fibril formation, and residues 8−20 have been recognized as another amyloidogenic region.[20,21] In the presence of a lipid membrane, the membrane binding and insertion of IAPP were reported to be initiated from its N-terminal part through electrostatic interaction.[8,22]

Received: November 6, 2014
Revised: February 2, 2015
Published: February 3, 2015

DOI: 10.1021/jp5111357
J. Phys. Chem. B 2015, 119, 3366−3376

CD spectra of $hIAPP_{1-19}$ and full-length hIAPP suggested that both peptides adopt a primarily α-helical structure in 1-palmitoyl-2-oleoyl-*sn*-glycero-3-phospho(1′-rac-glycerol) (POPG) lipid bilayers.[4,6] POPG liposome leakage experiments suggested that $hIAPP_{1-19}$ has the pathological membrane disrupting activity of the full-length hIAPP.[6] The rat version of $IAPP_{1-19}$ (rIAPP), despite differing from $hIAPP_{1-19}$ by only one residue (i.e., H18R mutation), was shown to be significantly less toxic than $hIAPP_{1-19}$.[23]

Although the secondary structure of IAPP/$IAPP_{1-19}$ monomers in a membrane environment has been extensively studied by experiments, their high-resolution three-dimensional (3D) structure in lipid bilayers has not been reported yet as NMR experiments could not be directly utilized in lipid bilayers due to the rapid aggregation of IAPP. All of the reported 3D structures were solved in sodium dodecyl sulfate (SDS) or dodecylphosphocholine (DPC) detergent micelles at different pHs using NMR spectroscopy, including the 3D structures of (1) $hIAPP_{1-37}$ (with the C-terminus being unamidated) in SDS micelles at pH 4.6,[24] (2) $hIAPP_{1-37}$ (with an amidated C-terminus) in SDS micelles at physiological pH,[25] (3) $rIAPP_{1-37}$ in DPC micelles at pH 7.3,[26] and (4) $hIAPP_{1-19}$ and $rIAPP_{1-19}$ in DPC micelles at pH 7.3.[27] For $h(r)IAPP_{1-19}$ species, its 3D structure in DPC micelles consisting of a single helix extending from C7 to V17 and a distorted helical turn from the N-terminus to C7.[27] The orientation of the peptide in the DPC micelle was reported to be pH-dependent. At pH 7.3, the $hIAPP_{1-19}$ peptide was buried deeper than the surface-bound $rIAPP_{1-19}$ counterpart, but protonating H18 in $hIAPP_{1-19}$ reoriented the peptide to the surface of the micelle.[27] As a micelle typically contains 50−80 detergent molecules, its small size and large curvature might have bias toward peptide conformations[15] and might also cause the position of peptides in micelles to be different from that in lipid bilayers.[25,28] For example, a recent experimental study on hIAPP aggregation in various membrane models (including SDS/DPC micelles, DHPC bicelles, and small/large unilamellar vesicles) suggested that SDS and DPC micelles stabilized the α-helical conformations of hIAPP, and no fibril formation was observed in these media.[29] Knowledge of structures of IAPP/$IAPP_{1-19}$ in lipid membranes is of great importance to understand their different extents of aggregation and toxicity; however, a comprehensive understanding of their 3D structures and their lipid interaction in anionic lipid bilayers at the atomic level are still missing.

On the computational side, a number of studies have explored the conformational ensembles of monomeric species of full-length IAPP[7,30−34] and the oligomeric species of different IAPP fragments (such as $IAPP_{20-29}$, $IAPP_{22-27}$, and $IAPP_{11-25}$)[35−38] in aqueous solution. Recently, investigations on the structures and orientations of $IAPP_{1-37}$[39−42] and $IAPP_{1-25}$[43] in neutral and/or anionic membranes have emerged. However, these simulations in a membrane environment all started from prebuilt membrane-bound/unbound preformed helical/β-sheet structures, and they were carried out at constant temperature, leading to insufficient conformational sampling. Thus, the obtained results might be biased by the initially preformed structures. In this study, we have performed replica exchange molecular dynamics (REMD) simulations using 48 replicas (400/500 ns per replica) with a explicit membrane on both human and rat $IAPP_{1-19}$ peptides. As a first step to understand the membrane-mediated $IAPP_{1-19}$ oligomerization, we chose the anionic POPG lipid bilayer as a model membrane system to study. To our knowledge, this is the first REMD simulation study on the human and rat $IAPP_{1-19}$ monomers in the presence of explicit lipid bilayers. On the basis of a ∼20 μs REMD simulation for each peptide started from a random coil conformation of the peptide placed in water, we find that unfolded $h(r)IAPP_{1-19}$ can insert into the POPG bilayer, and the membrane-bound peptides adopt coil conformations or amphiphatic helical structures lying flat at the interface of lipid hydrophilic heads and hydrophobic tails. $hIAPP_{1-19}$ exhibits higher helix propensity (particularly in the L12−L16 region) than $rIAPP_{1-19}$ most likely due to weaker peptide−membrane interaction and stronger intrapeptide interaction. The formation of an amphiphatic helix may facilitate the peptide−peptide interaction of $IAPP_{1-19}$ in the membrane, which is important for $IAPP_{1-19}$ aggregation and toxic oligomer formation. Our calculated lipid S_{CD} values in $IAPP_{1-19}$ + POPG and neat POPG systems are quite similar, indicating that $hIAPP_{1-19}$ and $rIAPP_{1-19}$ monomers do not cause membrane disruption, consistent with existing experimental results.[5,17] As oligomerization is crucial for membrane disruption, the structural difference and the different propensity to form amphiphatic helical structures for the two peptides in lipid bilayers may explain the more toxic property of $hIAPP_{1-19}$.

MATERIALS AND METHODS

Systems. The sequence of $h(r)IAPP_{1-19}$ is NH_3^+−KCNTA[5]TCATQ[10]RLANF[15]LVH(R)S−NH_2, with the Cys2 and Cys7 forming a disulfide bond and the C-terminus being amidated. The starting state of $hIAPP_{1-19}$ is a primarily random coil conformation, and that of $rIAPP_{1-19}$ is obtained by mutating H18 of $hIAPP_{1-19}$ into R18. The peptide is initially placed in water with a minimum distance from the bilayer surface of 1.3 nm (see Figure S1 in the Supporting Information). Our modeled lipid bilayer consists of 49 anionic POPG lipids per leaflet, built from an equilibrated bilayer with 64 lipids per leaflet from a previous computational study.[44] The peptide−membrane systems are solvated with simple point charge water. Na^+ and Cl^- ions are added to neutralize the charges of the peptide−membrane system and to provide an additional 120 mM salt concentration to be consistent with the NMR experiment condition.[27] More details about the system preparation are given in the Supporting Information.

REMD Simulations. The REMD method is an enhanced sampling method that reduces the time of the system trapped in local minima of the energy landscape, thus allowing a better sampling of the conformational landscape.[45] We have investigated the structural properties and membrane interactions of human and rat $IAPP_{1-19}$ peptides in an anionic phospholipid membrane by conducting extensive REMD simulations. We use 48 replicas at temperatures exponentially spaced between 310 and 455 K. The lowest temperature is chosen to be higher than the POPG gel−liquid crystalline phase transition temperature (≈274 K).[46] The simulation time for the $hIAPP_{1-19}$/$rIAPP_{1-19}$ system is 400/500 ns per replica. The peptides and POPG lipids are described using, respectively, Gromos87[47] and the Berger force field,[48] in accordance with our previous MD simulation studies on the interactions of full-length hIAPP with a POPG bilayer.[39,40] All simulations are performed with GROMACS 4.5.3 software package.[49] More simulations details[50−55] are given in the Supporting Information.

Constraints are usually applied to the lipid bilayer when simulated with REMD using the CHARMM force field for

DOI: 10.1021/jp5111357
J. Phys. Chem. B 2015, 119, 3366−3376

lipids[56,57] in order to prevent disintegration of the lipid bilayer at high temperature.[58,59] In our REMD simulations, we did not apply constraints to the lipid bilayer, as done previously by Ulmschneider et al.[60] Figure S2 (Supporting Information) shows that at 331 K, the membrane thickness decrease gradually with simulation time, and it reaches a plateau after 200 ns. We also monitor the variations of the area per lipid, the bilayer thickness, and the S_{CD} values of the sn-1 chain with temperature (Figure S3a−c, Supporting Information). It can be seen from this figure that the area per lipid of the POPG bilayer increases with temperature, while both the bilayer thickness and the S_{CD} values of the sn-1 chain (i.e., palmitoyl) decrease with temperature. These data indicate that compared to the membrane at 310 K, the lipid bilayer at higher temperatures inflates along the membrane plane and shrinks along the membrane normal. Nevertheless, it maintains the integrity of the lipid bilayer, as seen from a representative snapshot at 377 K in Figure S3d (Supporting Information).

Analysis Methods. All analyses have been carried out with our in-house-developed codes and GROMACS facilities. All results reported in this study refer to the REMD sampling collected at 331 K. The reasons for which we use the data at this temperature for analysis are given in the Supporting Information. We discarded the first 300/400 ns of each replica to remove the bias of the initial state for the hIAPP$_{1-19}$/rIAPP$_{1-19}$ peptide and used the last 100 ns of data for analysis. We analyzed the REMD data with several parameters, including the secondary structure content,[61] the z-position of each amino acid residue, the free-energy landscape, the number of hydrogen bonds (H-bonds), the salt bridges,[62] and main chain−main chain (MC−MC) and side chain−side chain (SC−SC) contact probability maps.[63] All of the representations of the studied systems are drawn with the VMD program.[64] A detailed description of these parameters is given in the Supporting Information.

RESULTS AND DISCUSSION

A 400/500 ns REMD simulation has been conducted on the hIAPP$_{1-19}$/rIAPP$_{1-19}$ system. Both peptides adsorb to the membrane surface within the first 25 ns and respectively stay at the water−lipid interface for 100 and 300 ns, as shown in Figure S4 (Supporting Information). After 135 ns, hIAPP$_{1-19}$ inserts into the bilayer and stays mostly at 0.3−0.8 nm below the phosphorus atoms (Figure S4a, Supporting Information). In contrast, rIAPP$_{1-19}$ takes more time to insert into the membrane due to its stronger electrostatic interactions with the lipid head groups as there is one more net positive charge in rIAPP$_{1-19}$. rIAPP$_{1-19}$ is located in the POPG bilayer at 0.3−0.8 nm below the phosphorus atoms after 310 ns (Figure S4b, Supporting Information). The peptide−membrane distance curves for both systems reach a plateau after 310 ns, indicating the convergence of the two REMD simulations.

The convergence of the REMD simulations is further verified by comparing the number of peptide−membrane H-bonds and the dominant secondary structure contents (including the helix, turn, bend, and coil) of each amino acid residue within two different time intervals using the 300−350 and 350−400 ns data for the hIAPP$_{1-19}$ system and the 400−450 and 450−500 ns data for the rIAPP$_{1-19}$ system (see Figures S5 and S6, Supporting Information). As shown in Figure S5 (Supporting Information), the number of protein−membrane H-bonds displays similar distributions within two different time intervals for both systems. As shown in Figure S6 (Supporting Information), the secondary structure contents of most of the residues within the two time windows are also quite similar for both systems, although the secondary structure probability of a few residues has certain differences. Overall, these data suggest that our two REMD simulations are reasonably converged over the last 100 ns. The convergence of our REMD simulations at 331 K indicates that analysis using the data generated at 331 K can provide an appropriate estimate to the conformational space of the peptide, and we do not need to reweigh all of the configurations at different temperatures, as shown recently by us[35,65,66] and many other groups.[67−69]

We then investigate the influence of IAPP$_{1-19}$ monomers on the ordering of the POPG bilayer by calculating the deuterium order parameter (S_{CD}).[70] The S_{CD} values of the sn-1 chain (i.e., palmitoyl) and sn-2 chain (i.e., oleoyl) are shown in Figure S7 (Supporting Information). For comparison, the S_{CD} values for a pure POPG bilayer are also given. For the first five carbon atoms, their S_{CD} values in the sn-1/sn-2 chain in the IAPP$_{1-19}$ + POPG system are the same/larger as/than those in a neat POPG bilayer system, indicating the ordering of these carbon atoms. By contrast, the S_{CD} values of the last eight/five carbons in the sn-1/sn-2 chain in the IAPP$_{1-19}$ + POPG system are smaller than those in a neat POPG bilayer system, indicating less ordering of these carbon atoms. For both acyl chains, the S_{CD} curves of POPG in hIAPP$_{1-19}$ + POPG and rIAPP$_{1-19}$ + POPG systems overlap well, indicating similar perturbation effects of human and rat IAPP$_{1-19}$ on the ordering of the POPG bilayer. Overall, the lipid S_{CD} values in IAPP$_{1-19}$ + POPG and neat POPG systems are quite similar, differing by only 0.05, indicating that hIAPP$_{1-19}$ and rIAPP$_{1-19}$ monomers do not cause membrane disruption, consistent with existing experimental results.[5,17]

hIAPP$_{1-19}$ and rIAPP$_{1-19}$ Monomers Display Different Secondary Structure Propensities in a POPG Bilayer. The calculated average probabilities of helix, turn, bend, and coil structures are, respectively, 10, 18, 18, and 53% for hIAPP$_{1-19}$ and 6, 19, 16, and 58% for rIAPP$_{1-19}$. The helix probability of hIAPP$_{1-19}$ is higher than that of rIAPP$_{1-19}$, while the coil probability is lower. The per residue secondary structure contents are also markedly different, as seen from Figure 1. Two dominant helical regions are observed in the hIAPP$_{1-19}$ peptide, namely, the N-terminal region spanning residues T4−T9 and the C-terminal region spanning residues L12−L16,

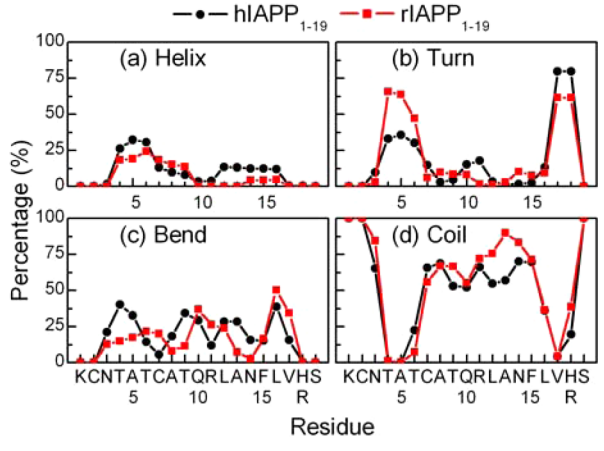

Figure 1. Secondary structure contents for hIAPP$_{1-19}$ (black curve) and rIAPP$_{1-19}$ (red curve) as a function of amino acid residue.

DOI: 10.1021/jp5111357
J. Phys. Chem. B 2015, 119, 3366−3376

while only the N-terminal helical region is seen in $rIAPP_{1-19}$ (see Figure 1a).

To compare the secondary structures of the two peptides in more details, we divide the whole peptide into five regions according to helical propensity: T4−T6, C7−C9, Q10−R11, L12−L16, and V17−H(R)18. As the three residues near the N-terminus, K1−N3, and the C-terminal residue S19 are mostly in coil structures, they are excluded here. It can be seen from Figure 1 that for the T4−T6 region, the percentages of helix and bend structures are larger for $hIAPP_{1-19}$ ($hIAPP_{1-19}$ versus $rIAPP_{1-19}$: 30 versus 21% for helix, 29 versus 18% for bend) due to the H18R mutation, while the turn propensity increases noticeably with the mutation (from 33 to 59%). For the C7−T9 region, the probability of helical structures is similar for the two peptides. In both peptides, residues Q10 and R11 mainly adopt coil (50−70%) and bend structures (10−40%). For the L12−L16 region, the helix percentage in $hIAPP_{1-19}$ (11−14%) is much higher than that in $rIAPP_{1-19}$ (<5%). Significant differences in secondary structure propensities are also seen for residues V17 and H18 around the mutation site. These two residues have a higher turn probability in $hIAPP_{1-19}$ (80%) than that in $rIAPP_{1-19}$ (62%). Most of the residues in both peptides have high propensities (>50%) to adopt coil structures except residues T4−T6 and L16−H(R)18 (Figure 1d). These results demonstrate that the H18R mutation decreases the helix propensity of residues L12−L16 and increases the turn propensity of residues T4−T9. The helix region found in our simulations is consistent with the NMR experiments of $hIAPP_{1-19}$ and $rIAPP_{1-19}$ in DPC micelles at neutral pH, where a helix encompassing residues C7−V17 was observed for both peptides.[27] Other experimental studies on the structures of the full-length IAPP in a mixed lipid (80% POPS/20% POPC) bilayer (using site-directed spin labeling and electron paramagnetic resonance (EPR) spectroscopy)[28] or in SDS detergent micelles at acidic and neutral pH conditions (using NMR spectroscopy)[24−26] also found helical structures running through the N-terminal region. It should be noted that the helix segment of $rIAPP_{1-19}$ found here is shorter than that of the solution NMR structure in DPC micelles. This difference in helix length might be due to the different model membrane used. Micelle models, including SDS and DPC, may overstabilize helical structures of IAPP,[29] thus leading to longer helices.

Conformational Ensembles and Free-Energy Landscapes of $hIAPP_{1-19}$ and $rIAPP_{1-19}$ in POPG Bilayers. To explore the dominant conformational states of human and rat $IAPP_{1-19}$ peptides in a POPG bilayer, we perform a RMSD-based cluster analysis for 25000 conformations for each system. Using a backbone RMSD of 0.1 nm, the conformations of $hIAPP_{1-19}$ and $rIAPP_{1-19}$ are separated into 43 and 36 clusters, respectively. The center structures of the top five most-populated clusters (C1−C5 for $hIAPP_{1-19}$ and C1′−C5′ for $rIAPP_{1-19}$) and their corresponding probabilities are given in Figure 2. These clusters represent 59 and 62% of the total conformations of $hIAPP_{1-19}$ and $rIAPP_{1-19}$ peptides, respectively. It can be seen from Figure 2a,b that $hIAPP_{1-19}$ has higher helical propensity than $rIAPP_{1-19}$. Helical structures are observed in clusters 2−4 of $hIAPP_{1-19}$, while they are only seen in a single cluster (C1′) of $rIAPP_{1-19}$. It is worth mentioning that the $hIAPP_{1-19}$ helix in cluster C2, spanning residues A5−L16, is much longer than the $rIAPP_{1-19}$ helix in C1′, consisting of residues T4−T9. Statistics on the secondary structures of all of the conformations in each cluster is shown in

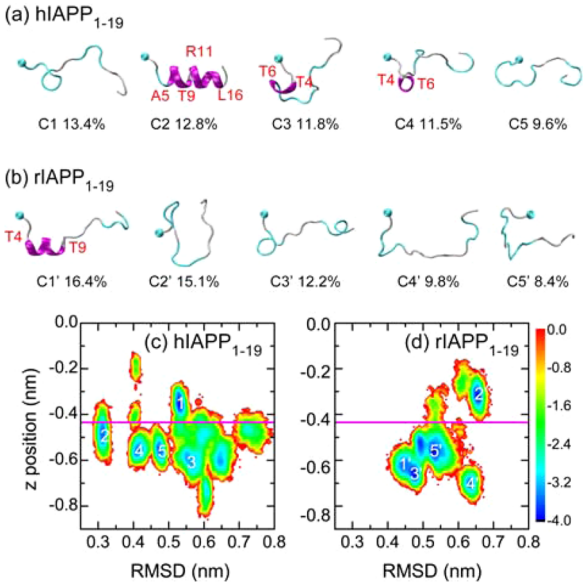

Figure 2. (a,b) Representative conformations of the top five most-populated clusters and the corresponding populations for $IAPP_{1-19}$. The peptide backbone is shown in cartoon representation (purple: helix; silver: coil; cyan: turn and bend.) The Cα atom of K1 is shown by a cyan bead. Free-energy landscape (in kcal/mol) for (c) $hIAPP_{1-19}$ and (d) $rIAPP_{1-19}$ in a POPG bilayer. Labels in the energy basins correspond to the cluster indexes. The purple line represents the average z-position of the first lipid tail carbon atoms in the upper leaflet. The average z-position of the upper leaflet phosphorus atoms is set to 0 (z = 0).

Figure S8 (Supporting Information). As seen from Figure S8b (Supporting Information), residues from A5 to L16 in C2 have higher propensities (≥60%) to adopt helical structures except for Q10 and R11 with turn structures. A short helix spanning residues T4−T6 is observed in 60% of all conformations in C3 and in nearly all conformations of C4. Conformations in C3 are the most compact, with the smallest end-to-end distance (1.67 ± 0.06 nm) among the five clusters. The conformations in the other two clusters (C1 and C5) of $hIAPP_{1-19}$ mainly adopt bend and coil structures, except that there is a turn from A5 to C7 in C1 (see Figure S8a, Supporting Information). Conformations in C1 are the most extended, with the largest end-to-end distance of 2.35 ± 0.06 nm among the five $hIAPP_{1-19}$ clusters.

The most populated conformation of $rIAPP_{1-19}$ is a partially helical structure containing a helix from T4 to T9 (see C1′ in Figure 2b) and has the longest end-to-end distance (2.70 ± 0.07 nm) among all of the 10 clusters shown in Figure 2. Conformations in C3′ and C4′ are also relatively extended, with end-to-end distances of 2.61 ± 0.03 and 2.51 ± 0.06 nm, respectively, but they are mostly in disordered coils and bends. The second largest cluster of $rIAPP_{1-19}$, that is, C2′, is an ensemble of disordered compact conformations with an end-to-end distance of 1.73 ± 0.04 nm. Conformations in C5′ are the most compact, with an end-to-end distance of 1.33 ± 0.03 nm. The helical conformations observed here for $hIAPP_{1-19}$ (C2) and $rIAPP_{1-19}$ (C1′) are consistent with the NMR-derived structures of the human/rat $IAPP_{1-19}$ fragment in DPC micelles. Detailed comparisons with experimental results are presented in the next section.

To have an overall view of the conformational ensembles and locations of human and rat $IAPP_{1-19}$ peptides in a POPG

DOI: 10.1021/jp5111357
J. Phys. Chem. B 2015, 119, 3366−3376

bilayer, we plotted in Figure 2c,d the free-energy landscape projected on two reaction coordinates: the C_α-RMSDs relative to, respectively, their NMR structures solved in DPC micelles[27] and the *z*-position of the centroid of the peptide backbone. We have labeled each energy basin using the index of the corresponding cluster, as shown in Figure 2 (for example, energy basin-1 corresponds to cluster-1). Basin-1 in Figure 2c and basin-2′ in Figure 2d are located, respectively, at (C_α-RMSD, *z*-position) values of (0.53 nm, 0.34 nm) and (0.66 nm, 0.31 nm). The peptide conformations that belong to these two energy basins are located at the hydrophilic region of the membrane (i.e., above the purple line). Other energy basins are primarily located at the hydrophobic region of the membrane (−0.51 to −0.75 nm for $rIAPP_{1-19}$ and −0.56 to −0.71 nm for $hIAPP_{1-19}$).

An earlier REMD simulation study demonstrated that a 16-residue peptide WALP16 can insert into the zwitterionic DPPC bilayer prior to helix formation and then fold inside of the membrane. Figure 2 shows that both $hIAPP_{1-19}$ and $rIAPP_{1-19}$ can exist in a coil conformation inside of the anionic POPG bilayer, indicating that these two peptides can insert into POPG bilayers mostly as an unfolded structure, similar to the WALP16 peptide.[58] To determine where the helix formation occurs, we first separate the trajectory into four independent time intervals: 0−100, 100−200, 200−300, and 300−400 ns. Then we plot in Figure S9 (Supporting Information) the probability density map of all of the conformations within each time interval as a function of the helix propensity of $hIAPP_{1-19}$ and the distance of the peptide to the bilayer center (d). As seen from Figure S9 (Supporting Information), within the initial 100 ns (0−100 ns), when $hIAPP_{1-19}$ is located in water (d = 2.6 nm) or just below lipid heads (d = 1.8 nm), the peptide has a very low probability to form a partially helical structure (with a helix propensity of ∼20%). Within the second 100 ns (i.e., 100−200 ns), $hIAPP_{1-19}$ stays mostly inside of membrane, and the conformations with partially helical structure increase, while hIAPP located in water does not show any helix signal. Within the 200−300 ns time interval, $hIAPP_{1-19}$ stays only inside of membrane, with the vast majority of the conformations being in unfolded states and a very small population of the conformations being in partially helical structure (with a helix propensity of ∼15%). Within the 300−400 ns time interval, the probability of partially helical structure increases, and the helix becomes longer (with a helix propensity of ∼45%). All of the helical conformations are located at a distance of 1.6 nm from the bilayer center (i.e., at the lipid head−tail interface). These data indicate that unfolded $hIAPP_{1-19}$ can insert into the POPG bilayer, with helix formation occurring when $hIAPP_{1-19}$ is located at the lipid head−tail interface. Similar behavior is observed for $rIAPP_{1-19}$ (data not shown).

For the conformations located in all of the energy basins, the C_α-RMSD values are in the range of 0.28−0.78 nm for $hIAPP_{1-19}$ (Figure 2c), while they vary from 0.41 to 0.67 nm for $rIAPP_{1-19}$ (Figure 2d). The wider C_α-RMSD value distribution suggests that $hIAPP_{1-19}$ samples a more diversified conformational space in the POPG bilayer than $rIAPP_{1-19}$ does. The helical conformations in C2 have the smallest C_α-RMSD (0.31 nm) with respect to the NMR structure of $hIAPP_{1-19}$ in DPC detergent micelles,[27] and they are located at the interface of lipid hydrophilic heads and hydrophobic tails. For $rIAPP_{1-19}$, the helical structures in C1′ have the smallest C_α-RMSD (0.45 nm) with respect to the NMR structure of $rIAPP_{1-19}$ in DPC micelles.[27] Such a large RMSD value mostly results from the disordered C-terminal residues Q10−S19. Combining the structures of $IAPP_{1-19}$ with the corresponding membrane burial depths, we conclude that the monomeric $hIAPP_{1-19}$/$rIAPP_{1-19}$ peptide is primarily located at an immersion depth of 0.3−0.8/0.2−0.8 nm below the phosphorus atoms of the POPG head groups. A previous experimental study suggested a helical preference for IAPP in the phosphorlipid head group region of the membrane.[5] Our results demonstrate that $IAPP_{1-19}$ has a preference to adopt helical structure when it is located at the interface of hydrophilic and hydrophobic regions of the POPG bilayer (see below for more detailed discussion). The anionic head groups of the POPG bilayer stabilize the intrapeptide electrostatic interactions by screening the positive charges of the peptide. Meanwhile, the lower dielectric constant of the lipid environment favors the formation of peptide backbone hydrogen bonds.[13] Also, the membrane tails provide a hydrophobic environment for the hydrophobic residues of the peptide. Thus, the amphiphilic interface of the POPG bilayer facilitates the folding of IAPP in the membrane.

Orientations of $hIAPP_{1-19}$ and $rIAPP_{1-19}$ Helical Structures in POPG Bilayers. As mentioned above, both $hIAPP_{1-19}$ and $rIAPP_{1-19}$ can adopt helical structures in a POPG bilayer. To probe the orientations of the helical structures in membrane, we present in Figure 3a,b the representative conformation of cluster-2 of $hIAPP_{1-19}$ and that of cluster-1′ of $rIAPP_{1-19}$ in a POPG bilayer. It is observed that the peptide is approximately parallel to the membrane surface. Quantitatively, the distribution of the angle of the $h(r)IAPP_{1-19}$ backbone with respect to the membrane surface in Figure 3c,d shows that the membrane-buried peptide has a tilt angle ranging from 5 to 18° for $hIAPP_{1-19}$ and 3 to 15° for $rIAPP_{1-19}$, revealing parallel orientation of $IAPP_{1-19}$ relative to the POPG bilayer surface.

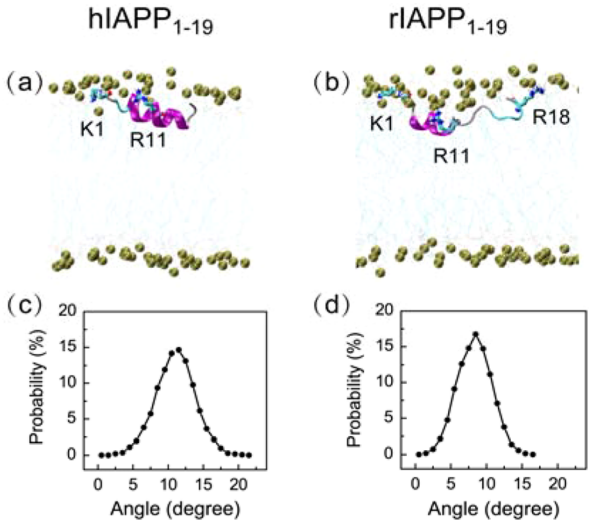

Figure 3. Representative helical structures of (a) $hIAPP_{1-19}$ and (b) $rIAPP_{1-19}$ in a POPG bilayer. The peptide backbone is shown in cartoon representation, colored by their secondary structures (purple: helix; cyan: turn and bend; silver: coil). All of the charged residues are emphasized using bond representation. The tan particles are the phosphorus atoms. (c,d) Distribution of the angle of the human and rat $IAPP_{1-19}$ backbone with respect to membrane surface.

We then examine the orientation of each amino acid residue in the helical structure of $IAPP_{1-19}$ peptide by calculating the *z*-

DOI: 10.1021/jp5111357
J. Phys. Chem. B 2015, 119, 3366−3376

position of each residue relative to the phosphorus atoms (z = 0). For $hIAPP_{1-19}$, as seen from Figure 4a, the helical structure

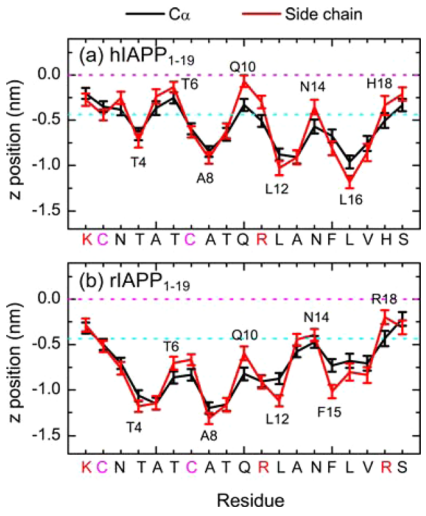

Figure 4. The z-position of the C_α atom and the side chain centroid of each residue in the helical structures of (a) $hIAPP_{1-19}$ and (b) $rIAPP_{1-19}$. The average z-positions of the phosphorus atoms and the first lipid tail carbon atom in the upper leaflet are shown, respectively, by the purple and cyan dotted lines.

is completely buried below the phosphorus groups, and its backbone is located at the interface of the hydrophilic head and hydrophobic tail regions of POPG bilayer (see the black curve in Figure 4a). Its centroid is at an immersion depth of ~0.7 nm, which is consistent with previous experimental study on $hIAPP_{1-37}$ in a 80% POPS/20% POPC bilayer that found the helix center to be at 0.6−0.9 nm below the lipid head groups.[28] The z-positions of side chains show that the side chains of hydrophilic residues T6, Q10, N14, and H18 are located at the hydrophilic lipid head region, while the side chains of hydrophobic residues A8, L12, and L16 fall into the hydrophobic lipid tail region, revealing that $hIAPP_{1-19}$ is an amphiphatic helix. Our finding is consistent with an earlier EPR spectroscopy study by Langen et al. on $hIAPP_{1-37}$ monomer in a mixed 80% POPS/20% POPC lipid bilayer, which reported that Q10, N14, and H18 fall into the hydrophilic face of the helix and the most deeply membrane-embedded residues T9, L12, L16, and S19 fall into the hydrophobic face. Our result is also in line with the data from MD simulations by Huo et al. on a preconstructed membrane-bound $hIAPP_{1-25}$ helix.[43] The amphiphatic feature of $hIAPP_{1-19}$ monomers inside of POPG bilayers may facilitate the peptide−peptide association inside of membranes via strong hydrophobic interactions. We note that the orientation of the membrane-embedded $hIAPP_{1-19}$ helical structure observed here is different from the orientation of $hIAPP_{1-37}$ adsorbed on the surface of the POPG bilayer membrane reported in our recent MD simulation study[40] due to the different locations of the peptide. Compared to the adsorption study of hIAPP at the membrane surface,[40] our current study goes one step beyond by providing the atomistic details of hIAPP after its insertion into the POPG bilayer.

Using spin-labeled lipids and EPR spectroscopy, Langen et al. found that residues T9, L12, L16, and S20 are at a relatively constant immersion membrane depth of 1.6 nm.[28] In our simulations, we find that the most deeply membrane-buried residues are A8, L12, and L16 (see the red curve in Figure 4a), consistent with the EPR study,[28] but they are at an immersion depth of 0.9−1.2 nm. The difference in membrane immersion depth is probably due to the different extent of negatively charged lipids in the model membrane. In Langen's experiment, the lipid bilayer consists of 80% POPS, while in our simulation, the lipid bilayer consists of 100% POPG, which may cause IAPP to have stronger electrostatic interaction with POPG head groups, leading to a smaller immersion depth in the POPG bilayer.

For $rIAPP_{1-19}$, as seen from Figure 4b, its C-terminal region from residues N14 to R18 is buried less deeply than its N-terminal region from T4 to R11, different from the case of $hIAPP_{1-19}$ (Figure 4a). This difference is attributed to the increased attractive electrostatic interactions between $rIAPP_{1-19}$ and the negatively charged lipid head groups of POPG lipids due to the H18R mutation. The $rIAPP_{1-19}$ peptide, albeit with lower helix content than $hIAPP_{1-19}$, also displays an amphiphatic feature, with the side chains of hydrophobic residues A8, L12, and F15 pointing toward the lipid tails and those of residues T6, Q10, N14, and R18 pointing toward the lipid heads. The NMR structures of $h(r)IAPP_{1-19}$ monomers in DPC micelles suggested that both human and rat $IAPP_{1-19}$ monomers are bound to the micelle surface.[27] The discrepancy in the location of $IAPP_{1-19}$ in the POPG bilayer and that in DPC micelle might result from the different curvatures of the POPG bilayer and DPC micelles as well as the different lipid compositions. It is noted that the 3D structures of $IAPP_{1-19}$ in anionic bilayers were not reported previously.

H18R Mutation Enhances the Peptide−Lipid Interaction while Weakening the Intrapeptide Interaction. We examine the peptide−lipid interactions by probing the salt bridge formation between the positively charged groups (i.e., the NH_3^+ group in the N-terminus (N-ter) and those in the side chains of K1, R11, and R18) of $IAPP_{1-19}$ and the negatively charged phosphate (PO_4^-) groups of POPG lipids. To this aim, we calculate the minimum distance between the two oppositely charged groups. As shown in Figure S10 (Supporting Information), the minimum distance between the NH_3^+ group of N-ter, K1, R11, or R18 and the PO_4^- group is smaller than 0.32 nm, indicating the formation of salt bridges. The distance distribution peaks of the N-ter−PO_4^- and K1−PO_4^- are located at a smaller distance than those of R11−PO_4^- and R18−PO_4^-, indicating stronger interactions between the N-terminus of $IAPP_{1-19}$ and the POPG bilayer. We find that the distance distribution peak of R11−PO_4^- in $rIAPP_{1-19}$ is shifted to the right located on the right of R18. This observation indicates that the H18R mutation weakens the interaction between R11 and phosphate groups while strengthening the interactions between R18 and phosphate groups.

We then calculate the numbers of H-bonds formed within the peptide and those between the peptide and lipid head (including glycerol, phosphate, and ester). The results are shown in Figure 5. For both $hIAPP_{1-19}$ and $rIAPP_{1-19}$, most of the intrapeptide hydrogen bonds are formed among the main chains (Figure 5a). We also observe H-bonds between the main chains and the side chains (Figure 5a), while there are very few H-bonds formed between the side chains (Figure 5b). Among the three groups of lipid heads, $IAPP_{1-19}$ mainly forms H-bonds with the phosphate and ester groups through its side chains. In contrast, there are few H-bonds between $IAPP_{1-19}$ and the glycerol group. Compared with $rIAPP_{1-19}$, $hIAPP_{1-19}$ has more intrapeptide H-bonds (11.6 versus 7.0), but it forms fewer H-

DOI: 10.1021/jp5111357
J. Phys. Chem. B 2015, 119, 3366−3376

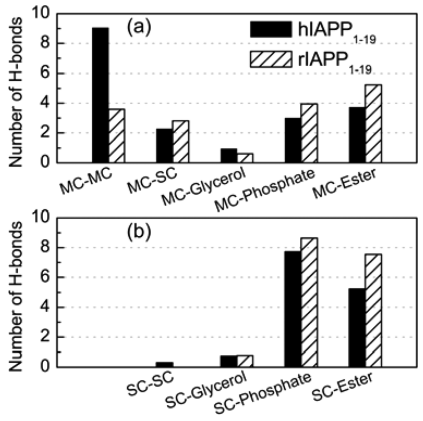

Figure 5. Number of hydrogen bonds formed by the (a) main chain (MC) and (b) side chain (SC) with each other, with themselves, and with three lipid groups (glycerol, phosphate, and ester) in helical structures (i.e., cluster-2) of $hIAPP_{1-19}$ and (cluster-1′) of $rIAPP_{1-19}$.

bonds with the lipids (21.1 versus 27.4). These data demonstrate that the intrapeptide hydrogen-bonding interactions of $rIAPP_{1-19}$ are weaker than those of $hIAPP_{1-19}$, while the peptide−lipid interactions between $rIAPP_{1-19}$ and POPG are stronger than those between $hIAPP_{1-19}$ and POPG.

To understand the physical forces that stabilize the helical and nonhelical structures of IAPP inside of POPG bilayers, we present in Table 1 the H-bond number and the total potential energy of the peptide in the top five most-populated clusters shown in Figure 2. The total potential energy includes the potential energy of the peptide itself (pep−pep) and the interaction energy between the peptide and its environment (including the membrane and water) (pep−mem and pep−wat). It can be seen from Table 1, for hIAPP, that the number of intrapeptide H-bonds of the helical structures in basin-2 is 12, much larger than the number of H-bonds of the nonhelical structures (≤7) in the other four basins. The pep−pep potential energy of helical structures is also lower than that of the nonhelical structures, indicative of the strongest intrapeptide interaction of the helical structures. Although the electrostatic interaction energy is much larger than the vdW interaction energy, the pep−pep energy difference between helical and nonhelical structures mainly comes from the vdW term. The strong pep−pep interaction (lower potential energy) of helical structures weakens the pep−mem interaction (higher potential energy) and reduces the number of H-bonds between the peptide and membrane. However, the number of H-bonds between the helical structures and the membrane is smaller than the number of H-bonds between the nonhelical structures and the membrane. The corresponding pep−mem interaction is also weaker than the interaction between the nonhelical structures and the membrane. For rIAPP, similar results are obtained, with the helical structures having more H-bonds, lower pep−pept energy, and higher pep−mem energy than the nonhelical structures. For both hIAPP and rIAPP, the pep−wat interaction energy is very small compared to the pep−mem term as there are very few water molecules in the membrane. The positive interaction energy between the peptide and water indicates that the interaction of water with the peptide is unfavorable for the peptide to stay inside of the membrane. Overall, the helical structures (in basin-2 for hIAPP and basin-1′ for rIAPP) have a lower total potential energy (see the most right column of Table 1) than the nonhelical structures in most of the basins. It should be noted that nonhelical structures in basin-4 of hIAPP and basin-5′ of rIAPP have lower total potential energy than the helical structures in basin-2 and basin-1′, respectively, due to the very strong pep−mem electrostatic interaction. Our previous MD study showed that the electrostatic interaction energy of a charged residue with a single lipid molecule is very large, ranging from −10 to −20 kJ/mol.[39] The lower potential energy of basin-4 and basin-5′ might be due to the local gathering of phosphates around the charged residues. Taken together, the potential energy analysis reveals that the helical structures are mostly favored by intrapeptide interactions, whereas the nonhelical structures are predominantly favored by peptide−membrane interactions.

To better understand the intrapeptide interactions, we have plotted in Figure 6 the contact probability maps for MC−MC and SC−SC pairs. The SC−SC contact probability map displays mostly local contacts that are regrouped into three dominant submatrices, spanning residues C2−C7 (matrix 1 or 1′), C7−L12 (matrix 2 or 2′), and N14−S19 (matrix 3 or 3′)

Table 1. Number of H-Bonds, Total Potential Energy, And Potential Energy Components for hIAPP in Basins 1−5 and rIAPP in Basins 1′−5′[a]

		H-bonds #		potential energy (kJ/mol)								
		pep−pep	pep−mem	pep−pep			pep−mem			pep−wat		
basin index				vdW	elec	vdW+elec	vdW	elec	vdW+elec	vdW	elec	total
hIAPP	1	4	28	−388	−2202	−2590	−1264	−6285	−7549	−63	−22	−10225
	2	12	21	−567	−2232	−2799	−1094	−6361	−7455	14	−116	−10355
	3	6	22	−372	−2212	−2584	−1287	−6068	−7355	−12	−56	−10007
	4	5	27	−413	−2123	−2536	−1287	−6670	−7957	−9	91	−10412
	5	7	26	−440	−2312	−2752	−1262	−5865	−7127	−12	19	−9872
rIAPP	1′	6	27	−435	−1967	−2402	−1350	−8132	−9482	35	130	−11718
	2′	4	32	−349	−1882	−2231	−1339	−8317	−9656	−28	202	−11712
	3′	5	27	−408	−1755	−2163	−1319	−8314	−9633	37	146	−11613
	4′	5	28	−350	−1963	−2313	−1470	−8056	−9526	51	203	−11584
	5′	1	31	−377	−1640	−2017	−1409	−8571	−9980	16	218	−11764

[a]The H-bond number includes the number of intrapeptide (pep−pep) H-bonds and the number of H-bonds formed between peptide and POPG membrane (pep−mem). The total potential energy includes the potential energy of the peptide itself (pep−pep) and the interaction energy between the peptide and its environment (including the membrane and water) (pep−mem and pep−wat). The potential energy components include van der Waals (vdW) and electrostatic (elec) interaction energies.

DOI: 10.1021/jp5111357
J. Phys. Chem. B 2015, 119, 3366−3376

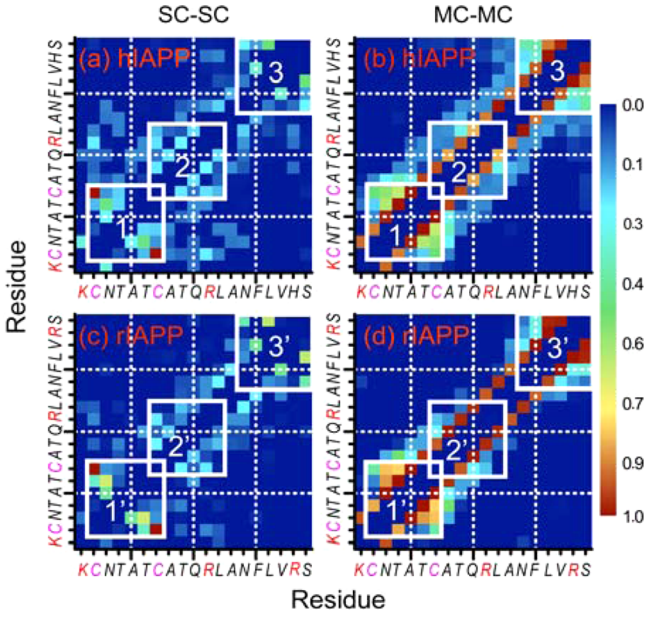

Figure 6. MC−MC and SC−SC contact probability maps of $hIAPP_{1-19}$ and $rIAPP_{1-19}$ peptides. For brevity, we use IAPP for $IAPP_{1-19}$ in this figure.

(Figure 6a,c). Due to the existence of a disulfide bond between C2 and C7, strong SC−SC and MC−MC interactions are observed between many pairs around this region for both $hIAPP_{1-19}$ and $rIAPP_{1-19}$ (i.e., matrix 1 and 1′). Strong MC−MC and SC−SC interactions are also observed between residue pairs in the region spanning residues N14−S19 for both peptides (i.e., matrix 3 and 3′). Within $hIAPP_{1-19}$, in the middle region (i.e., matrix 2 in (a) and (b)) of the peptide, the MC−MC and SC−SC interactions are still very strong for i−i+2 , i−i+3, i−i+4, and i−i+5 pairs. In contrast, within $rIAPP_{1-19}$, the SC−SC interactions in this region (i.e., matrix 2′ in Figure 6c) are dramatically weakened, and the MC−MC interactions are sharply reduced mainly for i−i+2 pairs (i.e., matrix 2′ in Figure 6d). This is consistent with the less ordered structure of this region in $rIAPP_{1-19}$ as indicated by the higher coil probability (Figure 1d) compared to that of the same segment in $hIAPP_{1-19}$.

Long-range interactions are also observed in $hIAPP_{1-19}$. For example, the side chain of H18 has contacts with those of residues T9, R11, L12, and N14 (Figure 6a). In contrast, the R18 side chain in $rIAPP_{1-19}$ has no contacts with any other residues (Figure 6c). Due to the fact that R11 is in the middle of the IAPP peptide, its side chain has an opportunity to interact with many of its neighboring residues. Differently, being at the terminus and positively charged, R18 in rIAPP has a preference to interact with the lipid head groups (Figure 5). Therefore, it has less opportunity to interact with other residues (Figure 6c). This leads to obvious differences of intrapeptide interactions between $rIAPP_{1-19}$ and $hIAPP_{1-19}$. Experimental studies suggested that electrostatic interactions between the N-terminal 1−19 region and anionic lipids play a key role in IAPP−membrane interactions.[4,10,11,71] Here, we observe that the H18R mutation enhances the electrostatic interactions of $IAPP_{1-19}$ with the membrane and imposes constraints on the flexibility of the peptide. As a result, the interactions of $rIAPP_{1-19}$ with the membrane are stronger than those of $hIAPP_{1-19}$, which is reflected by a larger number of hydrogen bonds formed with the membrane, which leads to weakened intrapeptide interactions within $rIAPP_{1-19}$ and thus a lower helical propensity compared to that of $hIAPP_{1-19}$. Several models have implied that the association of helix structures in the membrane plays an important role in the oligomerization of IAPP, which leads to a high local peptide concentration and facilitates the aggregation of IAPP.[9,25,72] Our simulations suggest that the enhanced protein−membrane interaction lowers the helix probability for $rIAPP_{1-19}$, which might disfavor the helix−helix association important for the full-length IAPP oligomerization in phospholipid membranes.[73] These results may explain the lower toxic property of $rIAPP_{1-19}$. The interaction of IAPP with the cellular membrane is believed to be crucial for its cytotoxic activity through catalyzing the formation of toxic oligomers.[12,13] As $hIAPP_{1-19}$ was reported to display pathological membrane-disrupting activity of the full-length peptide[6] and the N-terminal 1−19 region is crucial for helix−helix association, the results obtained here for $IAPP_{1-19}$ might provide molecular insights into the interactions of full-length IAPP with anionic lipid bilayers. Future studies are needed to investigate the structural properties of membrane-bound IAPP oligomers.

CONCLUSIONS

We have studied for the first time at the atomistic level the conformations, orientations, and membrane interactions of human and rat $IAPP_{1-19}$ monomers in anionic POPG bilayers by performing extensive REMD simulations started from a predominantly random coil conformation placed in the water environment. Our simulations demonstrate that both $hIAPP_{1-19}$ and $rIAPP_{1-19}$ peptides can insert into the POPG membrane in an unfolded conformation, with helix formation occurring after membrane insertion. Inside of the POPG bilayer, the two peptides can adopt amphiphatic helical structures and coil conformations, lying flat at the interface of lipid hydrophilic heads and hydrophobic tails. The potential energy analysis reveals that the helical structures are mostly favored by intrapeptide interactions, whereas the nonhelical structures are predominantly favored by peptide−membrane interactions. Secondary structure analysis shows that $hIAPP_{1-19}$ monomer has a higher probability to adopt helical structures than $rIAPP_{1-19}$. Two helical regions spanning residues T4−T9 and L12−L16 are observed in $hIAPP_{1-19}$, while only one helical region (residues T4−T9) is seen in $rIAPP_{1-19}$. The representative helical structure is characterized by an amphiphatic helix that is oriented parallel to the membrane surface with its hydrophilic residues facing the lipid head groups and the hydrophobic residues facing the lipid tail groups. Their structural differences and different propensities to form amphiphatic helical structures in lipid bilayers may affect the formation of the later oligomers of $IAPP_{1-19}$. We also find that more hydrogen bonds are formed between $rIAPP_{1-19}$ and the lipid hydrophilic head groups. As $rIAPP_{1-19}$ carries one more positive charge (due to H18R mutation) than $hIAPP_{1-19}$, the interactions of $rIAPP_{1-19}$ with the membrane are stronger, thus weakening the intrapeptide interactions. The relatively stronger intramolecular interactions in $hIAPP_{1-19}$ are beneficial for the formation of helical structures important for $IAPP_{1-19}$ oligomerization in phospholipid membranes. These results provide structural insights into the different oligomerization and membrane disruption propensities of human and rat $IAPP_{1-19}$ peptides.

DOI: 10.1021/jp5111357
J. Phys. Chem. B 2015, 119, 3366−3376

■ ASSOCIATED CONTENT

Supporting Information

Details of system preparation, REMD simulations, and analysis parameters, as well as 10 supplementary figures (Figures S1–S10), showing the initial structure of $hIAPP_{1-19}$ and $rIAPP_{1-19}$ with the POPG bilayer systems, the thickness of the POPG bilayer as a function of simulation time, the temperature dependence of the structural properties of a POPG bilayer, the distance from the centroid of the $hIAPP_{1-19}$ and $rIAPP_{1-19}$ peptide with respect to the bilayer center as a function of the simulation time, the percentage distribution of the number of hydrogen bonds between the peptide and the POPG membrane, secondary structure probabilities, time-averaged order parameters, secondary structure contents of the conformations, the probability density map averaged over all of the conformations, and the distribution of the minimum distance between the positively charged NH_3^+ groups of $IAPP_{1-19}$ and the negatively charged PO_4^- groups of POPG lipids. This material is available free of charge via the Internet at http://pubs.acs.org.

■ AUTHOR INFORMATION

Corresponding Author

*E-mail: ghwei@fudan.edu.cn.

Notes

The authors declare no competing financial interest.

■ ACKNOWLEDGMENTS

This work was supported by the National Natural Science Foundation of China (11074047 and 91227102). Simulations were performed at the National High Performance Computing Center of Fudan University and on the supercomputers of Calcul Quebec of the Université de Montréal. This work was also supported in part by the Canada Research Chairs program, the Fonds québecois de recherche sur la nature et les technologies (FQRNT), the Natural Sciences and Engineering Research Council of Canada (NSERC), and the Fonds de recherche en santé du Québec (FRSQ).

■ REFERENCES

(1) Cooper, G. J. S.; Willis, A. C.; Clark, A.; Turner, R. C.; Sim, R. B.; Reid, K. B. M. Purification and characterization of a peptide from amyloid-rich pancreases of type-2 diabetic-patients. *Proc. Natl. Acad. Sci. U.S.A.* **1987**, *84*, 8628–8632.

(2) Westermark, P.; Andersson, A.; Westermark, G. T. Islet amyloid polypeptide, islet amyloid, and diabetes mellitus. *Physiol. Rev.* **2011**, *91*, 795–826.

(3) Höppener, J. W.; Ahrén, B.; Lips, C. J. Islet amyloid and type 2 diabetes mellitus. *N. Engl. J. Med.* **2000**, *343*, 411–419.

(4) Jayasinghe, S. A.; Langen, R. Lipid membranes modulate the structure of islet amyloid polypeptide. *Biochemistry* **2005**, *44*, 12113–12119.

(5) Knight, J. D.; Hebda, J. A.; Miranker, A. D. Conserved and cooperative assembly of membrane-bound α-helical states of islet amyloid polypeptide. *Biochemistry* **2006**, *45*, 9496–9508.

(6) Brender, J. R.; Lee, E. L.; Cavitt, M. A.; Gafni, A.; Steel, D. G.; Ramamoorthy, A. Amyloid fiber formation and membrane disruption are separate processes localized in two distinct regions of IAPP, the type-2-diabetes-related peptide. *J. Am. Chem. Soc.* **2008**, *130*, 6424–6429.

(7) Reddy, A. S.; Wang, L.; Singh, S.; Ling, Y. L.; Buchanan, L.; Zanni, M. T.; Skinner, J. L.; de Pablo, J. J. Stable and metastable states of human amylin in solution. *Biophys. J.* **2010**, *99*, 2208–2216.

(8) Engel, M. F. M.; Yigittop, H.; Elgersma, R. C.; Rijkers, D. T. S.; Liskamp, R. M. J.; de Kruijff, B.; Hoppener, J. W. M.; Killian, J. A. Islet amyloid polypeptide inserts into phospholipid monolayers as monomer. *J. Mol. Biol.* **2006**, *356*, 783–789.

(9) Williamson, J. A.; Loria, J. P.; Miranker, A. D. Helix stabilization precedes aqueous and bilayer-catalyzed fiber formation in islet amyloid polypeptide. *J. Mol. Biol.* **2009**, *393*, 383–396.

(10) Knight, J. D.; Miranker, A. D. Phospholipid catalysis of diabetic amyloid assembly. *J. Mol. Biol.* **2004**, *341*, 117511–117587.

(11) Sasahara, K.; Hall, D.; Hamada, D. Effect of lipid type on the binding of lipid vesicles to islet amyloid polypeptide amyloid fibrils. *Biochemistry* **2010**, *49*, 3040–3048.

(12) Gurlo, T.; Ryazantsev, S.; Huang, C. J.; Yeh, M. W.; Reber, H. A.; Hines, O. J.; O'Brien, T. D.; Glabe, C. G.; Butler, P. C. Evidence for proteotoxicity in beta cells in type 2 diabetes toxic islet amyloid polypeptide oligomers form intracellularly in the secretory pathway. *Am. J. Pathol.* **2010**, *176*, 861–869.

(13) Matsuzaki, K.; Jayasinghe, S. A.; Langen, R. Membrane interaction of islet amyloid polypeptide. *Biochim. Biophys. Acta* **2007**, *1768*, 2002–2009.

(14) Hebda, J. A.; Miranker, A. D. The interplay of catalysis and toxicity by amyloid intermediates on lipid bilayers: insights from type II diabetes. *Annu. Rev. Biophys.* **2009**, *38*, 125–152.

(15) Butterfield, S. M.; Lashuel, H. A. Amyloidogenic protein membrane interactions: mechanistic insight from model systems. *Angew. Chem., Int. Ed.* **2010**, *49*, 5628–5654.

(16) Last, N. B.; Rhoades, E.; Miranker, A. D. Islet amyloid polypeptide demonstrates a persistent capacity to disrupt membrane integrity. *Proc. Natl. Acad. Sci. U.S.A.* **2011**, *108*, 9460–9465.

(17) Janson, J.; Ashley, R. H.; Harrison, D.; McIntyre, S.; Butler, P. C. The mechanism of islet amyloid polypeptide toxicity is membrane disruption by intermediate-sized toxic amyloid particles. *Diabetes* **1999**, *48*, 491–498.

(18) Mirzabekov, T. A.; Lin, M. C.; Kagan, B. L. Pore formation by the cytotoxic islet amyloid peptide amylin. *J. Biol. Chem.* **1996**, *271*, 1988–1992.

(19) Kayed, R.; Sokolov, Y.; Edmonds, B.; McIntire, T. M.; Milton, S. C.; Hall, J. E.; Glabe, C. G. Permeabilization of lipid bilayers is a common conformation-dependent activity of soluble amyloid oligomers in protein misfolding diseases. *J. Biol. Chem.* **2004**, *279*, 46363–46366.

(20) Jaikaran, E.; Higham, C. E.; Serpell, L. C.; Zurdo, J.; Gross, M.; Clark, A.; Fraser, P. E. Identification of a novel human islet amyloid polypeptide β-sheet domain and factors influencing fibrillogenesis. *J. Mol. Biol.* **2001**, *308*, 515–525.

(21) Goldsbury, C.; Goldie, K.; Pellaud, J.; Seelig, J.; Frey, P.; Muller, S. A.; Kistler, J.; Cooper, G. J.; Aebi, U. Amyloid fibril formation from full-length and fragments of amylin. *J. Struct. Biol.* **2000**, *130*, 352–362.

(22) Lopes, D. H.; Meister, A.; Gohlke, A.; Hauser, A.; Blume, A.; Winter, R. Mechanism of islet amyloid polypeptide fibrillation at lipid interfaces studied by infrared reflection absorption spectroscopy. *Biophys. J.* **2007**, *93*, 3132–3141.

(23) Brender, J. R.; Hartman, K.; Reid, K. R.; Kennedy, R. T.; Ramamoorthy, A. A single mutation in the nonamyloidogenic region of islet amyloid polypeptide greatly reduces toxicity. *Biochemistry* **2008**, *47*, 12680–12688.

(24) Patil, S. M.; Xu, S. H.; Sheftic, S. R.; Alexandrescu, A. T. Dynamic α-helix structure of micelle-bound human amylin. *J. Biol. Chem.* **2009**, *284*, 11982–11991.

(25) Nanga, R. P. R.; Brender, J. R.; Vivekanandan, S.; Ramamoorthy, A. Structure and membrane orientation of IAPP in its natively amidated form at physiological pH in a membrane environment. *Biochim. Biophys. Acta* **2011**, *1808*, 2337–2342.

(26) Nanga, R. P. R.; Brender, J. R.; Xu, J. D.; Hartman, K.; Subramanian, V.; Ramamoorthy, A. Three-dimensional structure and orientation of rat islet amyloid polypeptide protein in a membrane environment by solution NMR spectroscopy. *J. Am. Chem. Soc.* **2009**, *131*, 8252–8261.

DOI: 10.1021/jp5111357
J. Phys. Chem. B 2015, 119, 3366–3376

(27) Nanga, R. P. R.; Brender, J. R.; Xu, J. D.; Veglia, G.; Ramamoorthy, A. Structures of rat and human islet amyloid polypeptide IAPP(1−19) in micelles by NMR spectroscopy. *Biochemistry* **2008**, *47*, 12689−12697.
(28) Apostolidou, M.; Jayasinghe, S. A.; Langen, R. Structure of α-helical membrane-bound human islet amyloid polypeptide and its implications for membrane-mediated misfolding. *J. Biol. Chem.* **2008**, *283*, 17205−17210.
(29) Caillon, L.; Lequin, O.; Khemtémourian, L. Evaluation of membrane models and their composition for islet amyloid polypeptide−membrane aggregation. *Biochim. Biophys. Acta* **2013**, *1828*, 2091−2098.
(30) Dupuis, N. F.; Wu, C.; Shea, J.-E.; Bowers, M. T. Human islet amyloid polypeptide monomers form ordered β-hairpins: a possible direct amyloidogenic precursor. *J. Am. Chem. Soc.* **2009**, *131*, 18283−18292.
(31) Miller, C.; Zerze, G. H.; Mittal, J. Molecular simulations indicate marked differences in the structure of amylin mutants, correlated with known aggregation propensity. *J. Phys. Chem. B* **2013**, *117*, 16066−16075.
(32) Qiao, Q.; Bowman, G. R.; Huang, X. Dynamics of an intrinsically disordered protein reveal metastable conformations that potentially seed aggregation. *J. Am. Chem. Soc.* **2013**, *135*, 16092−16101.
(33) Wei, L.; Jiang, P.; Xu, W.; Li, H.; Zhang, H.; Yan, L.; Chan-Park, M. B.; Liu, X.-W.; Tang, K.; Mu, Y.; et al. The molecular basis of distinct aggregation pathways of islet amyloid polypeptide. *J. Biol. Chem.* **2011**, *286*, 6291−6300.
(34) Singh, S.; Chiu, C. C.; Reddy, A. S.; De Pablo, J. J. α-helix to β-hairpin transition of human amylin monomer. *J. Chem. Phys.* **2013**, *138*, 155101−155110.
(35) Qi, R.; Luo, Y.; Ma, B.; Nussinov, R.; Wei, G. Conformational distribution and α-helix to β-sheet transition of human amylin fragment dimer. *Biomacromolecules* **2014**, *15*, 122−131.
(36) Colombo, G.; Daidone, I.; Gazit, E.; Amadei, A.; Di Nola, A. Molecular dynamics simulation of the aggregation of the core-recognition motif of the islet amyloid polypeptide in explicit water. *Proteins* **2005**, *59*, 519−527.
(37) Mo, Y.; Lu, Y.; Wei, G.; Derreumaux, P. Structural diversity of the soluble trimers of the human amylin(20−29) peptide revealed by molecular dynamics simulations. *J. Chem. Phys.* **2009**, *130*, 125101−125106.
(38) Rivera, E.; Straub, J.; Thirumalai, D. Sequence and crowding effects in the aggregation of a 10-residue fragment derived from islet amyloid polypeptide. *Biophys. J.* **2009**, *96*, 4552−4560.
(39) Zhang, Y.; Luo, Y.; Deng, Y. H.; Mu, Y. G.; Wei, G. H. Lipid interaction and membrane perturbation of human islet amyloid polypeptide monomer and dimer by molecular dynamics simulations. *PLoS One* **2012**, *7*, e38191.
(40) Jia, Y.; Qian, Z. Y.; Zhang, Y.; Wei, G. H. Adsorption and orientation of human islet amyloid polypeptide (hIAPP) monomer at anionic lipid bilayers: implications for membrane-mediated aggregation. *Int. J. Mol. Sci.* **2013**, *14*, 6241−6258.
(41) Pannuzzo, M.; Raudino, A.; Milardi, D.; La Rosa, C.; Karttunen, M. α-helical structures drive early stages of self-assembly of amyloidogenic amyloid polypeptide aggregate formation in membranes. *Sci. Rep.* **2013**, *3*, 2781−2781.
(42) Poojari, C.; Xiao, D.; Batista, V. S.; Strodel, B. Membrane permeation induced by aggregates of human islet amyloid polypeptides. *Biophys. J.* **2013**, *105*, 2323−2332.
(43) Duan, M. J.; Fan, J.; Huo, S. H. Conformations of islet amyloid polypeptide monomers in a membrane environment: implications for fibril formation. *PLoS One* **2012**, *7*, e47150.
(44) Elmore, D. E. Molecular dynamics simulation of a phosphatidylglycerol membrane. *FEBS Lett.* **2006**, *580*, 144−148.
(45) Sugita, Y.; Okamoto, Y. Replica-exchange molecular dynamics method for protein folding. *Chem. Phys. Lett.* **1999**, *314*, 141−151.
(46) Wiedmann, T.; Salmon, A.; Wong, V. Phase-behavior of mixtures of DPPC and POPG. *Biochim. Biophys. Acta* **1993**, *1167*, 114−120.
(47) Gunsteren, W. F. v.; Berendsen, H. J. C. *Groningen molecular simulation (GROMOS) library manual*; Biomos: Groningen, The Netherlands, 1987; p 221.
(48) Berger, O.; Edholm, O.; Jahnig, F. Molecular dynamics simulations of a fluid bilayer of dipalmitoylphosphatidylcholine at full hydration, constant pressure, and constant temperature. *Biophys. J.* **1997**, *72*, 2002−2013.
(49) Pronk, S.; Pall, S.; Schulz, R.; Larsson, P.; Bjelkmar, P.; Apostolov, R.; Shirts, M. R.; Smith, J. C.; Kasson, P. M.; van der Spoel, D.; et al. GROMACS 4.5: A high-throughput and highly parallel open source molecular simulation toolkit. *Bioinformatics* **2013**, *29*, 845−854.
(50) Hess, B.; Bekker, H.; Berendsen, H. J. C.; Fraaije, J. G. E. M. LINCS: A linear constraint solver for molecular simulations. *J. Comput. Chem.* **1997**, *18*, 1463−1472.
(51) Miyamoto, S.; Kollman, P. A. SETTLE — An analytical version of the SHAKE and RATTLE algorithm for rigid water models. *J. Comput. Chem.* **1992**, *13*, 952−962.
(52) Patra, M.; Karttunen, M.; Hyvonen, M. T.; Falck, E.; Lindqvist, P.; Vattulainen, I. Molecular dynamics simulations of lipid bilayers: Major artifacts due to truncating electrostatic interactions. *Biophys. J.* **2003**, *84*, 3636−3645.
(53) MacCallum, J. L.; Bennett, W. F. D.; Tieleman, D. P. Transfer of arginine into lipid bilayers is nonadditive. *Biophys. J.* **2011**, *101*, 110−117.
(54) Bussi, G.; Donadio, D.; Parrinello, M. Canonical sampling through velocity rescaling. *J. Chem. Phys.* **2007**, *126*, 014101−014107.
(55) Kandt, C.; Ash, W. L.; Tieleman, D. P. Setting up and running molecular dynamics simulations of membrane proteins. *Methods* **2007**, *41*, 475−488.
(56) Feller, S. E.; Yin, D.; Pastor, R. W.; MacKerell, A. D. Molecular dynamics simulation of unsaturated lipid bilayers at low hydration: parameterization and comparison with diffraction studies. *Biophys. J.* **1997**, *73*, 2269−2279.
(57) Klauda, J. B.; Venable, R. M.; Freites, J. A.; O'Connor, J. W.; Tobias, D. J.; Mondragon-Ramirez, C.; Vorobyov, I.; MacKerell, A. D.; Pastor, R. W. Update of the CHARMM all-atom additive force field for lipids: Validation on six lipid types. *J. Phys. Chem. B* **2010**, *114*, 7830−7843.
(58) Nymeyer, H.; Woolf, T. B.; Garcia, A. E. Folding is not required for bilayer insertion: replica exchange simulations of an α-helical peptide with an explicit lipid bilayer. *Proteins* **2005**, *59*, 783−790.
(59) Lockhart, C.; Klimov, D. K. Alzheimer's Aβ10−40 peptide binds and penetrates DMPC bilayer: an isobaric−isothermal replica exchange molecular dynamics study. *J. Phys. Chem. B* **2014**, *118*, 2638−2648.
(60) Ulmschneider, M. B.; Doux, J. P. F.; Killian, J. A.; Smith, J. C.; Ulmschneider, J. P. Mechanism and kinetics of peptide partitioning into membranes from all-atom simulations of thermostable peptides. *J. Am. Chem. Soc.* **2010**, *132*, 3452−3460.
(61) Kabsch, W.; Sander, C. Dictionary of protein secondary structure — Pattern-recognition of hydrogen-bonded and geometrical features. *Biopolymers* **1983**, *22*, 2577−2637.
(62) Kumar, S.; Nussinov, R. Close-range electrostatic interactions in proteins. *ChemBioChem* **2002**, *3*, 604−617.
(63) Day, R.; Bennion, B. J.; Ham, S.; Daggett, V. Increasing temperature accelerates protein unfolding without changing the pathway of unfolding. *J. Mol. Biol.* **2002**, *322*, 189−203.
(64) Humphrey, W.; Dalke, A.; Schulten, K. VMD: Visual molecular dynamics. *J. Mol. Graph.* **1996**, *14*, 33−38.
(65) Luo, Y.; Ma, B.; Nussinov, R.; Wei, G. Structural insight into tau protein's paradox of intrinsically disordered behavior, self-acetylation activity, and aggregation. *J. Phys. Chem. Lett.* **2014**, *5*, 3026−3031.
(66) Xie, L.; Luo, Y.; Lin, D.; Xi, W.; Yang, X.; Wei, G. The molecular mechanism of fullerene-inhibited aggregation of Alzheimer's β-amyloid peptide fragment. *Nanoscale* **2014**, *6*, 9752−9762.

DOI: 10.1021/jp5111357
J. Phys. Chem. B 2015, 119, 3366−3376

(67) Larini, L.; Shea, J.-E. Role of β-hairpin formation in aggregation: the self-assembly of the amyloid-β(25−35) peptide. *Biophys. J.* **2012**, *103*, 576−586.
(68) Chen, A. a.; García, A. E. High-resolution reversible folding of hyperstable RNA tetraloops using molecular dynamics simulations. *Proc. Natl. Acad. Sci. U.S.A.* **2013**, *110*, 16820−16825.
(69) Jiang, F.; Wu, Y. D. Folding of fourteen small proteins with a residue-specific force field and replica-exchange molecular dynamics. *J. Am. Chem. Soc.* **2014**, *136*, 9536−9539.
(70) Vermeer, L. S.; de Groot, B. L.; Reat, V.; Milon, A.; Czaplicki, J. Acyl chain order parameter profiles in phospholipid bilayers: computation from molecular dynamics simulations and comparison with 2H NMR experiments. *Eur. Biophys. J.* **2007**, *36*, 919−931.
(71) Li, S.; Micic, M.; Orbulescu, J.; Whyte, J. D.; Leblanc, R. M. Human islet amyloid polypeptide at the air−aqueous interface: a Langmuir monolayer approach. *J. R. Soc. Interface* **2012**, *9*, 3118−3128.
(72) Soong, R.; Brender, J. R.; Macdonald, P. M.; Ramamoorthy, A. Association of highly compact type II diabetes related islet amyloid polypeptide intermediate species at physiological temperature revealed by diffusion NMR spectroscopy. *J. Am. Chem. Soc.* **2009**, *131*, 7079−7085.
(73) Liu, G.; Prabhakar, A.; Aucoin, D.; Simon, M.; Sparks, S.; Robbins, K. J.; Sheen, A.; Petty, S. A.; Lazo, N. D. Mechanistic studies of peptide self-assembly: transient α-helices to stable β-sheets. *J. Am. Chem. Soc.* **2010**, *132*, 18223−18232.

DOI: 10.1021/jp5111357
J. Phys. Chem. B 2015, 119, 3366−3376